The TESS light curve of AI Phoenicis

Maxted, P. F. L.; Gaulme, Patrick; Graczyk, D.; Hełminiak, K. G.; Johnston, C.; Orosz, Jerome A.; Prša, Andrej; Southworth, John; Torres, Guillermo; Davies, Guy R.; Ball, Warrick; Chaplin, William J

DOI:
10.1093/mnras/staa1662

Monthly Notices of the ROYAL ASTRONOMICAL SOCIETY

MNRAS **498,** 332–343 (2020) doi:10.1093/mnras/staa1662
Advance Access publication 2020 June 12

The TESS light curve of AI Phoenicis

P. F. L. Maxted,[1]★ Patrick Gaulme,[2] D. Graczyk,[3] K. G. Hełminiak,[3] C. Johnston,[4] Jerome A. Orosz,[5] Andrej Prša,[6] John Southworth,[1] Guillermo Torres,[7] Guy R. Davies,[8,9] Warrick Ball[8,9] and William J Chaplin[8,9]

[1]*Astrophysics group, Keele University, Keele, Staordshire ST5 5BG, UK*
[2]*Max-Planck-Institut für Sonnensystemforschung, Justus-von-Liebig-Weg 3, D-37077 Göttingen, Germany*
[3]*Nicolaus Copernicus Astronomical Center, Polish Academy of Sciences, ul. Rabiańska 8, PL-87-100 Toruń, Poland*
[4]*Instituut voor Sterrenkunde, KU Leuven, Celestijnenlaan 200D, B-3001 Leuven, Belgium*
[5]*Astronomy Department, San Diego State University, 5500 Campanile Drive, San Diego, CA 92182-1221, USA*
[6]*Villanova University, Department of Astrophysics and Planetary Science, 800 Lancaster Avenue, Villanova, PA 19085, USA*
[7]*Center for Astrophysics, Harvard & Smithsonian, 60 Garden Street, Cambridge, MA 02138, USA*
[8]*School of Physics and Astronomy, University of Birmingham, Birmingham B15 2TT, UK*
[9]*Stellar Astrophysics Centre (SAC), Department of Physics and Astronomy, Aarhus University, Ny Munkegade 120, DK-8000 Aarhus C, Denmark*

Accepted 2020 June 8. Received 2020 June 6; in original form 2020 March 20

ABSTRACT

Accurate masses and radii for normal stars derived from observations of detached eclipsing binary stars are of fundamental importance for testing stellar models and may be useful for calibrating free parameters in these model if the masses and radii are sufficiently precise and accurate. We aim to measure precise masses and radii for the stars in the bright eclipsing binary AI Phe, and to quantify the level of systematic error in these estimates. We use several different methods to model the Transiting Exoplanet Survey Satellite (TESS) light curve of AI Phe combined with spectroscopic orbits from multiple sources to estimate precisely the stellar masses and radii together with robust error estimates. We find that the agreement between different methods for the light-curve analysis is very good but some methods underestimate the errors on the model parameters. The semi-amplitudes of the spectroscopic orbits derived from spectra obtained with modern échelle spectrographs are consistent to within 0.1 per cent. The masses of the stars in AI Phe are $M_1 = 1.1938 \pm 0.0008\,\mathrm{M}_\odot$ and $M_2 = 1.2438 \pm 0.0008\,\mathrm{M}_\odot$, and the radii are $R_1 = 1.8050 \pm 0.0022\,\mathrm{R}_\odot$ and $R_2 = 2.9332 \pm 0.0023\,\mathrm{R}_\odot$. We conclude that it is possible to measure accurate masses and radii for stars in bright eclipsing binary stars to a precision of 0.2 per cent or better using photometry from TESS and spectroscopy obtained with modern échelle spectrographs. We provide recommendations for publishing masses and radii of eclipsing binary stars at this level of precision.

Key words: binaries: eclipsing – stars: fundamental parameters – stars: individual: AI Phe – stars: solar-type.

1 INTRODUCTION

AI Phe is a moderately bright ($V = 8.6$) star that was first noted as an eclipsing binary by Strohmeier (1972). Photometric monitoring by Reipurth (1978) established that the orbital period is approximately 24.59 d and that the primary eclipse is total. Hrivnak & Milone (1984) obtained UBVRI light curves of AI Phe, covering both eclipses and combined their analysis of these light curves with the spectroscopic orbits for both stars published by Imbert (1979) to measure the masses and radii of both components. They found that the stars in AI Phe are slightly more massive than the Sun, and both have evolved away from the zero-age main sequence, with the more massive star being a subgiant. A much-improved spectroscopic orbit for AI Phe was published by Andersen et al. (1988) together with a re-analysis of the UBVRI light curves by Hrivnak & Milone (1984) and new *uvby* light curves, and a spectroscopic estimate of the metal abundance ([Fe/H] $= -0.14 \pm 0.1$). The analysis by Andersen et al. has been the definitive observational study of AI Phe until recently and the absolute parameters derived therein have often been used as a benchmark for testing stellar evolution models of single stars (e.g. Andersen et al. 1988; Pols et al. 1997; Ribas, Jordi & Giménez 2000; Lastennet & Valls-Gabaud 2002; Spada et al. 2013; Ghezzi & Johnson 2015; Higl & Weiss 2017).

Kirkby-Kent et al. (2016) used light curves obtained during the WASP exoplanet transit survey together with improved spectroscopic orbits for both components by Hełminiak et al. (2009) to improve the precision of the radius measurements for both components of AI Phe to better than 1 per cent. Sybilski et al. (2018) also obtained spectroscopic orbits for both components of AI Phe together with spectroscopic observations obtained during the secondary eclipse that show that the rotation axis of the subgiant component is not aligned with the orbital axis of the binary system. Gallenne et al. (2019) have used the VLTI interferometer to measure the astrometric

★ E-mail: p.maxted@keele.ac.uk

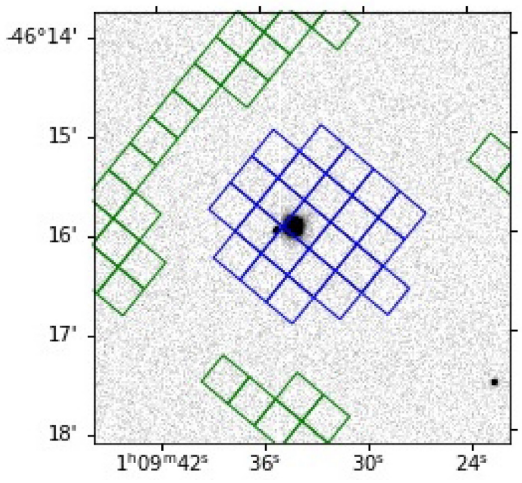

Figure 1. Skymapper r'-band image of AI Phe overlaid with the aperture used to calculate the TESS light curve of AI Phe. Pixels used to measure the flux are plotted in blue and pixels used to calculate the background value are plotted in green. The Skymapper data are displayed as an inverse logarithmic grey-scale image.

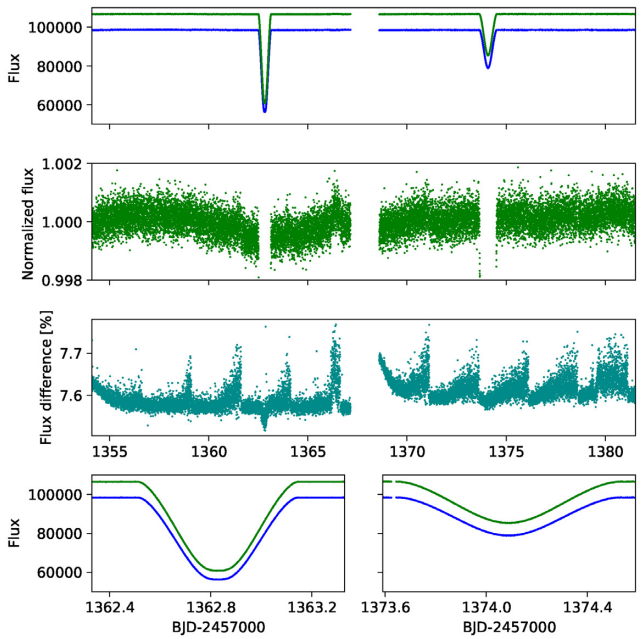

Figure 2. The TESS light curve of AI Phe. The lower (blue) curves show the SAP_FLUX values and the upper (green) curves shows the PDCSAP_FLUX values from the MAST archive data file. Only the PDCSAP_FLUX values are shown in the second panel down from the top. The flux difference value shown in the third panel down are $1 - SAP\_FLUX/PDCSAP\_FLUX$. Only data with a QUALITY flag value of 0 are shown in this figure.

orbit of AI Phe. They used this astrometric orbit combined with their own high-quality spectroscopic orbits for the two stars to derive their masses with a precision of better than 0.1 per cent and a model-independent distance to the binary of 169.4 ± 0.7 pc.

The duration of the primary and secondary eclipses of AI Phe are approximately 15 and 20 h, respectively. This, combined with the long orbital period of AI Phe, makes it difficult to obtain complete light curves from ground-based observatories. For any mid-latitude observing site it will be necessary to patch together eclipses observed on different nights, or even from different observing seasons, to obtain complete coverage of both eclipses. Kirkby-Kent et al. (2016) found that the orbital period of AI Phe is not constant, presumably due to the presence of a third body in the system. The orbit of the presumed third body is not well characterized, so it is possible that there is a systematic error in the published radius estimates for this binary due to inaccuracies in the orbital phases assigned to different parts of the light curve. This problem of phasing the light curve may explain the small discrepancies between the values of the orbital eccentricity, e, and longitude of periastron, ω, obtained in different studies (Kirkby-Kent et al. 2016).

The launch of the Transiting Exoplanet Survey Satellite (TESS; Ricker et al. 2015) afforded us the opportunity to obtain a high-precision light curve of AI Phe with complete coverage of both eclipses observed over a single orbital period of the binary system. Accordingly, we applied for and were awarded guest-observer status to observe AI Phe using the 2-min cadence mode of TESS (G011130, P.I. Maxted; G011083, P.I. Hełminiak; G011154, P.I. Prša). TESS is designed to produce very high-quality photometry of bright stars (100 ppm per hour or better for stars with $I_c \approx 8$) and AI Phe shows very well-defined total eclipses, so we expect a very small random error on the parameters derived from the analysis of the TESS light curve. Light curves for eclipsing binary stars of this quality have only become available within the past few years, so it is not yet clear to what extent the parameters derived are affected by systematic errors due to the methods used for the analysis. In order to get a better understanding of these systematic errors, we present here several independent analyses of the TESS light curve of AI Phe conducted by researchers using a variety of different software packages that they have previously used to analyse light curves of eclipsing binary stars. We also compile and compare the published spectroscopic orbits for AI Phe, both with each other and, where possible, to parameters derived from the light-curve analysis. These results are then combined to obtain accurate mass and radius estimates for both components in AI Phe to a precision of better than 0.2 per cent.

2 TESS LIGHT-CURVE ANALYSIS

The sky region around AI Phe is shown in Fig. 1 overlaid with the location of the pixels in the TESS images that are used to calculate the TESS light curve. The faint star to the east of AI Phe that is included in the TESS photometric aperture is listed in the TESS input catalogue (TIC) as TIC 616203794 with an estimated magnitude in the TESS band of $T = 13.67$. The estimated magnitude of AI Phe listed in the TIC is $T = 7.96$, so this faint companion contributes only about 0.5 per cent to the total flux measured by TESS. The pixels used to estimate the background level in the TESS images do not contain any stars brighter than $T = 13.5$.

TESS observations of AI Phe took place from 2018-08-22 to 2018-09-20 (Sector 2). The TESS light-curve files downloaded from the Mikulski Archive for Space Telescopes (MAST) contain two measurements of the flux labelled SAP_FLUX and PDCSAP_FLUX. SAP_FLUX light curves are the result of simple aperture photometry, i.e. the total counts measured within the photometric aperture from the calibrated TESS images corrected for the estimated background flux. PDCSAP_FLUX light curves include a correction to remove instrumental systematic variations by fitting and removing those signals that are common to all stars on the same detector. The SAP_FLUX and PDCSAP_FLUX light curves for AI Phe are shown

Table 1. Summary of models and optimization methods.

Run	Investigator	Model	Optimization	Limb darkening	Detrending	Notes
A	Maxted	`ellc`	EMCEE	Power-2	Celerite	
B	Hełminiak	JKTEBOP	L-M	Quadratic	Sine+poly	Monte Carlo error estimates.
C	Torres	EB	EMCEE	Quadratic	Spline	Quadratic l.d. coefficients fixed
D	′	′	′	′	′	
E	Graczyk	WD2007	L-M	Logarithmic	–	Fixed l.d. coefficients
F	Johnston	PHOEBE 1.0	EMCEE	Square root	–	
G	Prša	PHOEBE 2.1	MCMC	Grid	Legendre	
H	Orosz	ELC	DE-MCMC	Logarithmic	Polynomial	
I	Orosz	′	′	Square root	′	
J	Orosz	′	′	Quadratic	′	
K	Southworth	JKTEBOP	L-M	Quadratic	Polynomial	
L	Southworth	JKTEBOP	L-M	Cubic	Polynomial	
S	Maxted	`ellc`	EMCEE	Power-2	Celerite	Same as Run A with `SAP_FLUX`

Table 2. Geometric and orbital parameters derived from the analysis of the TESS light curve of AI Phe. The values in the final row are the mean and sample standard deviation for all runs. The time of primary eclipse, T_0 is given as $\mathrm{BJD_{TDB}} - 2458362$.

Run	$r_1 = R_1/a$	$r_2 = R_2/a$	$r_1 + r_2$	$k = r_2/r_1$	i (°)	$e\cos\omega$	$e\sin\omega$	T_0
A	0.037660(56)	0.061301(63)	0.09896(9)	1.6278(27)	88.356(6)	−0.065160(9)	0.1768(7)	0.82847(1)
B	0.037696(57)	0.061181(81)	0.09888(11)	1.6230(27)	88.368(7)	−0.065176(14)	0.175(1)	0.82834(1)
C	0.037724(28)	0.061253(57)	0.09898(5)	1.6240(24)	88.357(6)	−0.065167(8)	0.1762(6)	0.82835(1)
D	0.037700(62)	0.061285(73)	0.09900(11)	1.6257(29)	88.358(7)	−0.065156(13)	0.177(1)	0.82833(1)
E	0.037671(09)	0.061239(16)	0.09891(1)	1.6256(8)	88.359(3)	−0.065175(2)	0.1753(1)	0.82840(3)
F	0.03773(2)	0.06127(1)	0.09900(2)	1.6240(8)	88.351(1)	−0.06518(1)	0.1748(2)	0.82845(5)
G	0.03773(3)	0.06123(4)	0.09896(5)	1.6227(9)	88.351(9)	−0.065194(1)	0.17523(5)	0.82849(1)
H	0.037641(58)	0.061172(69)	0.09882(14)	1.6259(27)	88.361(6)	−0.065172(16)	0.1749(12)	0.82849(2)
I	0.037670(50)	0.061201(61)	0.09887(10)	1.6248(21)	88.360(6)	−0.065176(17)	0.1755(14)	0.82849(1)
J	0.037618(52)	0.061153(67)	0.09875(10)	1.6260(20)	88.365(6)	−0.065182(16)	0.1744(16)	0.82849(1)
K	0.037688(32)	0.061263(74)	0.09895(8)	1.6255(26)	88.359(7)	−0.065161(10)	0.1765(8)	0.82834(1)
L	0.03778(10)	0.06136(12)	0.09914(18)	1.6242(42)	88.352(10)	−0.065144(22)	0.1778(18)	0.82834(1)
S	0.037605(60)	0.061280(60)	0.09889(9)	1.6296(29)	88.357(6)	−0.065158(9)	0.1765(7)	0.82848(1)
–	0.037686(49)	0.061242(60)	0.09893(10)	1.6252(19)	88.359(6)	−0.065170(14)	0.1758(1)	0.82842(7)

in Fig. 2. The light-curve files also include a QUALITY flag for each measurement. In this study, we only use data with QUALITY = 0, i.e. for which there are no known issues with the measurement. Of the 19 737 flux measurements for AI Phe in the TESS light-curve file, 18 303 (93 per cent) have QUALITY = 0. The meta-data provided with the MAST light-curve file includes a parameter `CROWDSAP` that gives the ratio of the target flux to the total flux in the photometric aperture. For the AI Phe data, this has the value 0.999 932 35, so we assume that the contamination of the aperture by TIC 616203794 has not been accounted for in the creation of the `PDCSAP_FLUX` light curve.

In the following subsections, we describe in detail the various binary star models, optimization methods and parameter error estimation techniques that we have used to analyse the TESS light curve of AI Phe. The methods are summarized in Table 1. In all of the following descriptions, star 1 ('primary star') is the F7 V star that is totally eclipsed at phase 0 ('primary eclipse') by star 2 ('secondary star') the K0 IV star. We use the usual notation $r_i = R_i/a$ where r_i is the 'fractional radius' of star i, R_i is the actual radius of star i, and a is the semimajor axis of the binary orbit. The TESS light curve of AI Phe obtained during TESS Cycle 1 contains only one eclipse of each type, so it is not possible to determine the orbital period from these observations. For all of the light-curve analysis methods described below we fixed the orbital period at the nominal value $P = 24.5924$ d, close to the value obtained by Kirkby-Kent et al. (2016) from WASP observations of AI Phe obtained from 2006 to 2011.

2.1 Run A – Maxted, `ellc`

For Run A, we used version 1.8.5 of the binary star model `ellc`[1] (Maxted 2016) to fit the `PDCSAP_FLUX` light curve. We used the option available in this version of `ellc` to use the power-2 limb-darkening law (Hestroffer 1997; Maxted 2018b) for both stars. The trends in the data were first removed by fitting a simple Gaussian process (GP) model to the data between the eclipses in 1-h bins using the `celerite` software package (Foreman-Mackey et al. 2017) and then dividing the measured fluxes by the best-fitting GP model evaluated at all times of observation.

The free parameters in the fit are: a flux scaling factor, f; the sum of the fractional radii, $r_{\rm sum} = r_1 + r_2 = (R_1 + R_2)/a$; the ratio of the radii, $k = R_2/R_1$; the surface brightness ratio averaged over the stellar disks in the TESS band, $S_{\rm T}$; the orbital inclination, i; the time of primary eclipse, T_0; $f_s = \sqrt{e}\sin(\omega)$ and $f_c = \sqrt{e}\cos(\omega)$; 'third light', ℓ_3; the parameters of the power-2 limb-darkening law for star 1, $h_{1,\rm F}$, and $h_{2,\rm F}$; the parameters of the power-2 limb-darkening law for star 2, $h_{1,\rm K}$ and $h_{2,\rm K}$; the standard error per observation, σ_f.

We used table 2 from Maxted (2018b) to estimate the following limb-darkening parameters – $h_{1,\rm F} = 0.818$, $h_{2,\rm F} = 0.420$, $h_{1,\rm K} = 0.770$, $h_{2,\rm K} = 0.424$. We used Gaussian priors centred on these values with standard deviation of 0.05 and 0.25 for the h_1 and h_2 parameters,

[1] https://github.com/pmaxted/ellc

Table 3. Additional parameters derived from the analysis of the TESS light curve of AI Phe and the rms of the residuals from the best fits. A ⋆ symbol in the final column denotes runs that only included data in the region of the eclipses in the fit.

Run	e	ω (°)	ℓ_3	rms (ppm)	
A	0.1884(7)	110.23(8)	0.006(2)	356	⋆
B	0.1871(11)	110.39(13)	0.010(2)	416	
C	0.1878(6)	110.30(6)	0.008(2)	368	
D	0.1883(10)	110.24(11)	0.007(2)	368	
E	0.1870(7)	110.40(1)	0.007(1)	428	⋆
F	0.1866(1)	110.45(1)	0.006(4)	390	⋆
G	0.1859(4)	110.54(5)	0.007(2)	372	
H	0.1866(12)	110.40(16)	0.025(25)	353	⋆
I	0.1875(15)	110.41(12)	0.025(25)	353	⋆
J	0.1862(11)	110.48(12)	0.025(25)	353	⋆
K	0.1881(8)	110.27(9)	0.0053(25)	381	⋆
L	0.1894(17)	110.12(19)	0.0072(35)	381	⋆
S	0.1881(7)	110.27(8)	0.005(2)	364	⋆
–	0.1875(9)	110.34(11)	0.011(8)	–	–

respectively. Based on the results in Maxted (2018b), we expect the tabulated values to be much more accurate than these rather generous priors. The light traveltime across the orbit was included in the model assuming $a = 47.868\,\mathrm{R}_\odot$ (Borkovits et al. 2015). We used EMCEE (Foreman-Mackey et al. 2013), a PYTHON implementation of an affine invariant Markov chain Monte Carlo (MCMC) ensemble sampler to calculate the PPD of the model parameters. In order to speed up the calculation, we assumed that the stars are spherical and used the 'default' grid size for both stars. Another speed-up we used is to only calculate 1-in-4 observations using the `ellc` model and then to use linear interpolation to calculate intervening observations. To estimate the numerical noise in our light curves we compared a light curve computed with these settings to one computed with the 'very-fine' grid size and evaluated at every observed point. The root mean square (rms) residual of the difference through the eclipses is 33 ppm, about 10 times less than the standard error per observation. The oblateness of both stars is very small (< 0.08 per cent) so the use of spheres to approximate their shapes is very reasonable in this case.

The PPD was sampled using 1000 steps and 256 walkers following a 'burn-in' phase of 1000 steps. The light curve was analysed in two sections, each centred on an eclipse and with a width approximately twice the eclipse width. The convergence of the chain was evaluated by-eye from plots of parameters values versus step number. The typical autocorrelation length of the chains is about 70 steps so we thinned the chains by 100 steps before calculating the mean and standard deviation of the parameters given in Tables 2 and 3. The best-fitting model light-curve fit to the data used in the EMCEE analysis is shown in Fig. 3. Parameter correlation plots are shown in Fig. 4.

2.2 Run B – Hełminiak, JKTEBOP

The analysis for Run B was done using JKTEBOP[2] version 34 (Southworth 2013, and references therein). This code uses the Levenberg–Marquardt algorithm (Press et al. 1992) to optimize the

[2]JKTEBOP is written in FORTRAN77 and the source code is available at `http://www.astro.keele.ac.uk/jkt/codes/jktebop.html`.

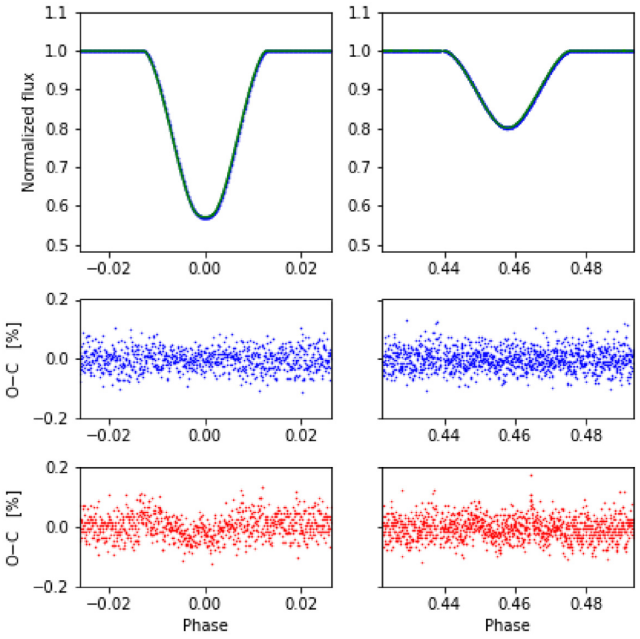

Figure 3. Upper panel: Best-fitting model from Run A (green line) for the TESS light curve of AI Phe (blue points). Middle panel: Residuals from the best-fitting model for Run A. Lower panel: Residuals from the best-fitting model for Run E.

parameters of the EBOP light curve model (Etzel 1981; Popper & Etzel 1981) from a least-squares fit to a light curve (`PDCSAP_FLUX`) expressed in magnitudes. We used the quadratic limb-darkening law option for both stars. The integration ring size used for numerical integration of the observed fluxes was 1 deg. This is sufficient to reduce numerical noise to less than 10 ppm.

The free parameters in the least-squares fit for Run B are J (the central surface brightness ratio), k, $r_{\rm sum}$, i, e, ω, ℓ_3, T_0, m_0 (magnitude zero-point), and the coefficients of the quadratic limb-darkening law for both stars. The parameter J is defined as the ratio of the surface brightness at the centre of the stellar discs, rather than the disc-average value $S_{\rm T}$ used for Run A. The residuals from an initial fit to the data were analysed using a Lomb–Scargle periodogram (Press et al. 1992). From this periodogram two significant frequencies corresponding to periods near 26 d and 2.4 d were identified. The 2.4-d periodicity is due to 'momentum dump' events when the space craft reaction wheel speeds are periodically reset to low values. This can be seen in the difference between the `PDCSAP_FLUX` and `SAPFLUX` values shown in Fig. 2.

We include sine waves with these two frequencies in the least-squares fit to the data together with a third-degree polynomial to model an additional trend seen in the residuals near the start of the data set. JKTEBOP includes options to modulate the flux of either star using these sine waves and polynomials, or to simply apply these trends as an overall scaling factor. We found that there is very little difference in the results for different combinations of these options so here we only quote the results for applying them as an overall scaling factor. We kept the frequency of the sine waves fixed at the values determined from the periodogram but their phases and amplitudes were included as free parameters in the fit, together with the coefficients of the third-degree polynomial.

All data were equally weighted in the least-squares fit and the errors on the parameters were estimated using a Monte Carlo simulation assuming Gaussian uncorrelated noise with the same

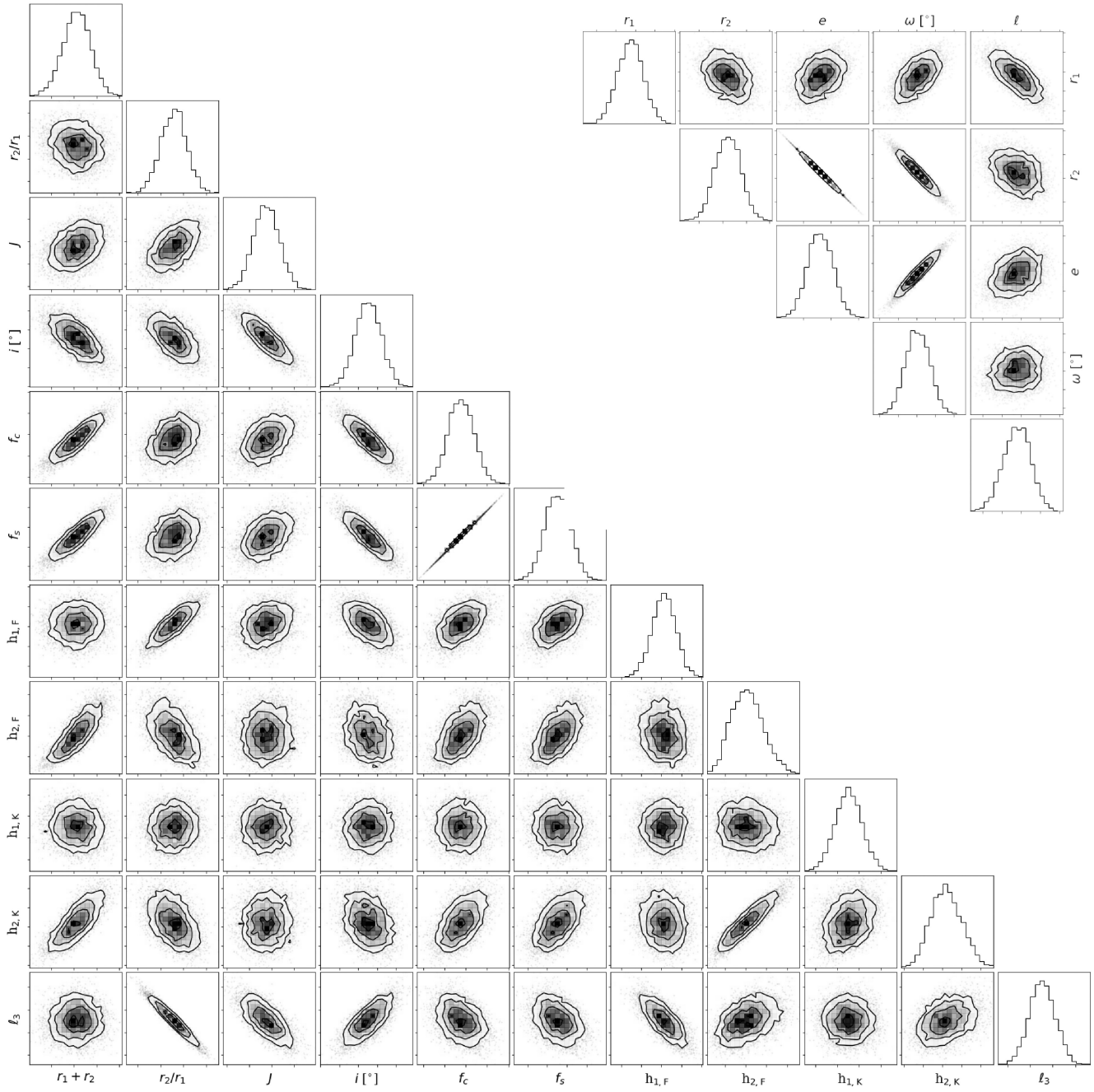

Figure 4. Parameter correlation plots for selected parameters from Run A. Model parameters not shown in this corner plot (f and σ_f) do not show any strong correlation with the other model parameters shown here. Parameter correlations are shown in the upper-right corner for quantities derived from the model parameters, including $\ell = S_T \times k^2 = 1.3212 \pm 0.0054$, the flux ratio in the TESS band.

standard deviation as the rms residual from the best fit. We checked these error estimates using the prayer-bead Monte Carlo method, which tended to give slightly lower error estimates. The parameters of the sine and polynomial detrending functions were kept fixed at their best-fitting values during these Monte Carlo simulations.

2.3 Runs C and D – Torres, EB

For Runs C and D the light-curve analysis used the PDCSAP_FLUX photometry, and was done with the EB program of Irwin et al. (2011), an improved version of the original EBOP light curve model, combined with EMCEE to explore the model parameter space. With the default integration ring size in EB the contribution of numerical noise to the computed light curves is ≈30 ppm or less. Trends in the data were removed by dividing thorough by a spline fit by least squares to the data between the eclipses, so computation of the ellipsoidal and reflection effects in the light curve were disabled. The free parameters in both fits were J, k, $r_{\rm sum}$, $\cos i$, $f_s = \sqrt{e}\sin(\omega)$, $f_c = \sqrt{e}\cos(\omega)$, ℓ_3, T_0, and $\ln f_\sigma$, where f_σ is a scaling factor for the errors on each measurement.

For Run C we used a quadratic limb-darkening law for both stars with the linear coefficients as free parameters and the quadratic coefficients fixed at the values for the TESS band of 0.3107 and 0.2162 for stars 1 and 2, respectively (Claret & Bloemen 2011). For Run D, we used the transformed limb-darkening parameters q_1 and q_2 defined by Kipping (2016) to efficiently sample the dependence of the posterior probability distribution (PPD) on both quadratic limb-darkening coefficients for both stars. Light traveltime within the binary was accounted for in the analysis, adopting the value 100.27 km s^{-1} for the sum of the radial velocity (RD) semi-amplitudes, from Hełminiak et al. (2009). The sampling of the PPD was done using 100 walkers and 40 000 steps following a burn-in phase with 35 000 steps. The results shown in Tables 2 and 3 were calculated from the mode of the posterior distributions and the 1σ errors based on half the range between the 16th and 84th percentiles.

2.4 Run E – Graczyk, WD2007

For Run E, we used the Wilson–Devinney (WD) light-curve model version WD2007 (Van Hamme & Wilson 2007) with 8392 grid points for both stars and logarithmic limb-darkening laws for both stars. We used the Cousins I_C band as an approximation to the TESS photometric passband and set the secondary star effective temperature to 5086 K. The free parameters in the least-squares fit are the effective temperature of the primary star, the values of the potentials defining the size and shapes of each star, the orbital inclination, e and ω, ℓ_3, a flux-scaling factor and a phase shift relative to the nominal time of mid-eclipse. The mass ratio used to calculate the Roche potential was $q = M_2/M_1 = 1.04017$. The data were normalized using a spline fit to PDCSAP_FLUX values between the eclipses. Only data in the region of the eclipses (2274 observations) were included in the analysis. The best-fitting model parameters were found by repeated application of the differential corrections calculated by WD2007. To estimate the numerical noise in our final model light curve, we compared it to a light curve computed with the same model parameters but a much finer grid spacing. In the regions of the eclipse, the rms difference between these two light curves is 140 ppm.

The radii quoted here are the arithmetic means of the radii at the side, pole, and substellar point of the Roche equipotential surfaces. A Monte Carlo calculation was used to calculate the standard errors for quantities derived from the free parameters of the model, assuming that their joint probability distribution is a multivariate Gaussian distribution. The covariance matrix for this multivariate Gaussian distribution was derived from the correlation matrix and parameter standard deviations provided in the output from WD2007. Some small systematic trends (∼300 ppm) are seen in the residuals from the fit to primary eclipse (Fig. 3). This is likely to be a consequence of using Cousins I_C band as an approximation to the TESS band for both the interpolation the limb-darkening coefficients and for the calculation of the flux ratio from the effective temperatures of both stars.

2.5 Run F – Johnston, PHOEBE 1.0

PHOEBE 1.0 is an enhanced version of the widely used WD light-curve model. It incorporates simple reflection, parametrized limb darkening, and gravity darkening, amongst other physics (Prša & Zwitter 2005). We used a square-root limb-darkening law with coefficients for the TESS passband interpolated from a pre-calculated grid of coefficients for each model. We increased the fine-grid resolution for the PHOEBE model by a factor of 3 compared to the standard grid size in the original WD model in order to better reproduce the points of ingress and egress. We adopted the solution of Kirkby-Kent et al. (2016) as our starting solution and determined errors using the ensemble MCMC sampling code EMCEE (Foreman-Mackey et al. 2013). We fixed the gravity darkening coefficients, period, and primary effective temperature to the value from Kirkby-Kent et al. To estimate the numerical noise in our final model light curve we compared it to a light curve computed with the same model parameters but a much finer grid spacing. In the regions of the eclipse, the rms difference between these two light curves is 126 ppm.

We did not include RVs in our fit but, in order to propagate forward any influence of a varying mass ratio, we applied a Gaussian prior on this parameter according to the value by Kirkby-Kent et al. (2016). Additionally, we sampled the reference time of mid-eclipse T_0, $\cos i$, $e\cos\omega$, $e\sin\omega$, the secondary effective temperature, the primary and secondary potentials and luminosities, and the third light. We fitted the PDCSAP_FLUX light curve provided by MAST with no further detrending. We used 128 chains and ran the algorithm for 10 000 iterations. We ensured solution convergence by running the sampler for at least five times the autocorrelation time of all parameter chains. We discarded all iterations before convergence as part of the burn-in phase.

2.6 Run G – Prša, PHOEBE 2.1

PHOEBE 2 (Prša et al. 2016) is a redesigned modelling suite for computing observable stellar properties that extends the previous version by adding missing physics and by increasing modelling fidelity. All technical and computational considerations are described in Prša (2018), including tests that were done to demonstrate that there is very little numerical noise in the light curves computed with this model.

The light curve of AI Phe was detrended by fitting a chain of fifth-order Legendre polynomials connected at data gaps to the sigma-clipped out-of-eclipse regions. PHOEBE 2.1 was used to build a model. Direction-dependent emergent intensities for each surface element were computed from Castelli & Kurucz (2003) model atmospheres; limb darkening was interpolated on a grid of 72 μ vertices from Castelli & Kurucz atmospheres synthesized by the spectrum code (Gray 1999); reflection/irradiation included both heating and scattering components explained in Horvat et al. (2018). The eccentricity and argument of periastron were replaced with their orthogonalized components, $e\cos\omega$ and $e\sin\omega$. The adjusted parameters include the time of superior conjunction, orbital inclination, effective temperature ratio, passband luminosity, third light contribution in the TESS passband, orthogonalized eccentricity and argument of periastron, and the sum and ratio of stellar radii. Initial parameter optimization was done using Nelder and Mead's Simplex method (Prša & Zwitter 2005), and solution sampling was done using Markov Chain Monte Carlo sampler EMCEE (Foreman-Mackey et al. 2013). Convergence was assessed by the Gelman–Rubin criterion (Gelman & Rubin 1992). In total, 128 walkers were used over a little over 10^5 iterations. Integrated surface brightness and flux ratios are computed at phase 0.25.

2.7 Runs H, I, and J – Orosz, ELC

Runs H, I, and J are identical except that a different limb-darkening law was used in each case, as listed in Table 1. The light curve was analysed in two sections, each centred on an eclipse and with a width approximately twice the eclipse width. A fifth-order polynomial fit by least-squares to the data either side of each eclipse was used to

divide-through all the data in each section so that the mean level out-of-eclipse was 1. The final adopted light curve has $N = 2193$ measurements with a median uncertainty per observation of 348 ppm. We used the ELC code (Orosz & Hauschildt 2000) to model the light curve. ELC has been modified to use the technique of Short et al. (2018) for the fast computation of eclipses of spherical stars. The tolerance settings in the numerical integrator used in ELC are set such that numerical noise in these light curves is well below 1 ppm. We used the optimiser available in ELC based on the DE-MCMC algorithm (Ter Braak 2006) for the results presented here. Similar runs using the optimiser based on the nested sampling algorithm (Skilling et al. 2006) gave similar results but with much smaller errors on the parameters. The primary temperature was fixed at $T_1 = 6310$ K. The free parameters in the fit were the inclination i, the time of primary eclipse T_0, the temperature ratio T_2/T_1, the sum of the fractional radii $r_1 + r_2$, the difference of the fractional radii $r_1 - r_2$, $e\cos\omega$, $e\sin\omega$, ℓ_3, and the four limb-darkening coefficients, two for each star. The temperature ratio is used to calculate the central surface brightness ratio, J, by integration of a model spectral energy distribution for each star over the TESS passband. For the analysis of a single light curve, this is equivalent to including J as a free parameter.

For each run, 50 chains were used and the chains were allowed to evolve for 100 000 generations. The chains were allowed to 'burn in' for 1000 generations. Thereafter, the posterior sample was constructed by using every thousandth generation. The uniform priors imposed on the model parameters generally span a much larger range than the width of posterior distribution. The exception is third light for which we found the posterior was approximately a uniform sampling of the prior $\ell_3 = [0, 0.05]$.

2.8 Runs K and L – Southworth, JKTEBOP

For these runs, we used version 38 of the JKTEBOP code, which differs only in small ways from version 34 used for Run B. We present results for the cases where limb darkening was implemented using the quadratic law (Run K) and the cubic law ($I(\mu) = 1 - u(1 - \mu) - v(1 - \mu)^3$; Run L) – the two runs are the same in all other respects. We also tried square-root limb darkening, finding that the results were very similar but the coefficients were highly correlated; logarithmic limb darkening, for which the correlations were so high the fit failed to converge quickly; and linear limb darkening, which we found to be inadequate for the current data. See Southworth (2008) for the definitions of the limb-darkening laws used.

We obtained the TESS light curve of AI Phe and converted it to magnitude units. We rejected the data more than twice the eclipse duration away from an eclipse mid-point, in order to speed up the fits to the data. We fitted for the sum and ratio of the fractional radii ($r_{\rm sum}$ and k), the orbital inclination (i), the central surface brightness ratio (J), the strength of the reflection effects for the stars, and the time of the mid-point of the primary eclipse (T_0). Third light (ℓ_3) was also included as a fitted parameter because of the presence of the fainter nearby star: we found a small value for ℓ_3 that was nevertheless significant at the 2σ level. All fits included two first-order polynomials to model the out-of-eclipse brightness of the system, one for each eclipse, as detrending functions.

Theoretical values for the quadratic limb-darkening coefficients of the two stars in the TESS passband were obtained from Claret (2017). Cubic limb-darkening coefficients are not available from this source so were obtained by fitting the quadratic trend with the cubic law. Initial fits for both quadratic and cubic limb darkening showed good results when the limb-darkening coefficients were fixed at these theoretical values. For the quadratic law, we obtained a significant improvement when fitting for the linear coefficient for each star ($\Delta\chi^2 = 220$), but no further improvement when fitting for both coefficients for each star ($\Delta\chi^2 = 0.2$). For the cubic law, the values are $\Delta\chi^2 = 228$ and 5.5, respectively. In both cases, all limb-darkening coefficients were physically realistic and measured with reasonable precision. We conclude that the theoretical coefficients are clearly worse than the fitted values, and that it is necessary to fit for at least one limb-darkening coefficient for each star. Our final results are given for the cases where the two linear limb-darkening coefficients are fitted using the quadratic law (Run K) and all four limb-darkening coefficients are fitted using the cubic law (Run L).

Fits were made to the data using the Levenberg–Marquardt method (Press et al. 1992). We tried values of the integration ring size from 0.2 to 5 deg. This change had a negligible effect on the results so we used a size of 5 deg for the final fits. The formal uncertainties from the covariance matrix often underestimate the true uncertainties, so we obtained parameter uncertainties in two other ways. First, we used 1000 Monte Carlo simulations (Southworth, Maxted & Smalley 2004). Secondly, we used the residual-permutation algorithm implemented in JKTEBOP (Southworth 2008). The final error bar for each parameter is the larger of the two options for that parameter, and in most cases, this comes from the residual-permutation simulations.

The final results for Runs K and L are shown in Tables 2 and 3. The differences between the best-fitting values for the two runs are due only to the treatment of limb darkening. The larger error bars for Run L versus Run K are because of the inclusion of four rather than two limb-darkening coefficients as fitted parameters.

2.9 Run S – Maxted, `ellc`

According to the TESS archive manual, at times the fitting method used to remove instrumental trends from the `SAP_FLUX` measurements is known to remove true astrophysical signals from the `PDCSAP_FLUX` values. In order to better understand if this is a problem for the TESS light curve of AI Phe, we repeated Run A using `SAP_FLUX` measurements instead of `PDCSAP_FLUX`.

3 ASTEROSEISMIC NON-DETECTION

We have searched the TESS light curves for signatures of solar-like oscillations from both components. We used the same analysis as described in Davies & Miglio (2016) to search for the characteristic pattern of modes of oscillation in the periodogram of the TESS light curve after dividing through the model of the eclipsing binary from Run A. All searches returned posterior distributions consistent with the prior distribution which we use as evidence for a non-detection of modes of oscillation, i.e. the TESS data provides no constraint on the asteroseismic properties of AI Phe.

An asteroseismic non-detection at this apparent magnitude for these two stars is consistent with predictions (i.e. Schofield et al. 2019). Fig. 5 shows the TESS periodogram together a simulated asteroseismic data set generated following Ball et al. (2018). In order to find stellar properties to input into the asteroseismic simulation, we used MESA (r10398, Paxton et al. 2018). We optimized to match the observed properties by varying the common age, common initial chemical composition, and individual mixing length parameters. While the details of the periodogram in Fig. 5 will be sensitive to the above procedure, the broad large-scale details are insensitive to the choices made above, and at the level of detail displayed, are expected to be accurate.

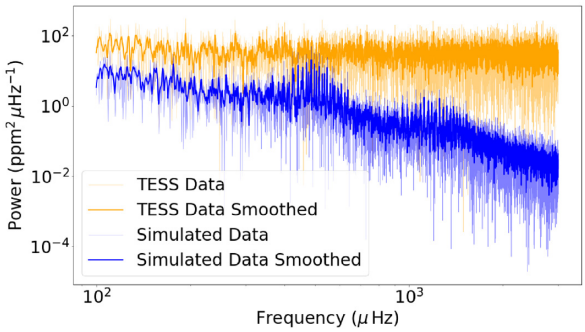

Figure 5. TESS periodogram and simulated noiseless asteroseismic periodogram for AI Phe.

The simulated data, in the absence of noise, clearly show two broad humps of modes at around 500 and 1050 μHz. While the highest frequency hump associated with the primary star is substantially lower than the noise floor, the modes of the secondary star are predicted to be close to the TESS AI Phe noise levels. A robust asteroseismic detection of the secondary would require a sizeable reduction in the noise levels and/or an extended temporal baseline for the observational time series.

Despite the non-detection here, AI Phe remains an excellent target for testing or calibrating asteroseismology, especially given the very high-precision observations given above. The PLATO mission (Rauer et al. 2014) will provide a larger effective aperture compared with TESS and as such will have significantly reduced noise levels. At a level of 200 ppm per cadence, which is indicative of what we might expect with PLATO, we would expect to detect high-quality asteroseismic signals from both components of AI Phe.

4 MASSES AND RADII

Hełminiak et al. (2009), Sybilski et al. (2018), and Gallenne et al. (2019) have all published spectroscopic orbits for both stars based on RVs measured from spectra with good signal-to-noise ratio (S/N $\gtrsim$ 30) obtained on échelle spectrographs with a resolving power $R \gtrsim 60\,000$. The spectroscopic orbit by Gallenne et al. (2019) was determined from a simultaneous fit to 33 RVs obtained with the HARPS spectrograph together with the astrometric orbit fit to measurements of the relative positions of the two stars obtained with the VLTI interferometer. The HARPS RVs were first corrected for the motion of the binary system due to a third body in the system with a long, eccentric orbit around AI Phe ($P_3 \gtrsim 100$ y, $e \sim 0.8$). As Gallenne et al. (2019) note the agreement between the parameters derived from these three independent studies is extraordinarily good. We used the following weighted-mean values for the semi-amplitudes to calculate the masses and radii of AI Phe: $K_1 = 51.164 \pm 0.007$ km s^{-1} and $K_2 = 49.106 \pm 0.010$ km s^{-1}.

The parameters of interest for the calculation of the masses and radii are $r_1 = R_1/a$, $r_2 = R_2/a$, $\sin i$, and e. From Tables 2 and 3, we see that the sample standard deviation across the analysis runs is similar to the typical error estimate for each parameter. We therefore decided to use the mean value of each parameter given in Table 2 to calculate the masses and radii of the stars. From Fig. 6, we see that some of these parameters are correlated so we used a Monte Carlo approach to calculate errors and covariances for the masses and radii. We used EMCEE to obtain 50 000 randomly sampled values from a multivariate normal distribution with the same mean and covariance matrix as the input values of r_1, r_2, $\sin i$, and e. These 50 000 sets of parameters were paired with the same number of K_1 and K_2 values from two independent normal distributions. For the orbital period, we used the value $P = 24.5924$ d and assumed that the error in this value is negligible. We then used equations and constants from Prša et al. (2016) to calculate the masses and radii of the stars in nominal solar units for every set of randomly sampled parameters. We also calculated the mean stellar density and surface gravity for each star. The mean and sample standard deviation of these random samples are given in Table 4 and the parameter correlation plots for the PPDs are shown in Fig. 7.

5 DISCUSSION

5.1 Consistency checks

A valuable test for the presence of unrecognized systematic errors is to compare values determined independently from separate data sets. In particular, e and ω are determined from the spectroscopic orbit and light curve independently to good precision. The values of $e\cos\omega$ and $e\sin\omega$ from the spectroscopic orbits of Sybilski et al. (2018) and Gallenne et al. (2019) are compared to the values obtained from the light curve in Fig. 6. A detailed statistical comparison of these values is not straightforward because there will be some covariance between these parameters from the spectroscopic orbit, and the values obtained from the light curve are affected by systematic errors. Nevertheless, by-eye there appears to be good agreement between these values obtained from spectroscopy and photometry. The values of $e\cos\omega$ and $e\sin\omega$ from Hełminiak et al. (2009) are also consistent with the values from the light-curve analysis and the two other spectroscopic orbits, although with significantly larger error bars.

The inclination of the binary orbit determined from the astrometric orbit by Gallenne et al. (2019) is also consistent with the value of i determined from the light curve, once the ambiguity in the sign of $\cos i$ determined from the light curve is accounted for. This is a less stringent check because of the relatively large error in the astrometric value.

One check that is not yet possible is to compare these results to those from the analysis light curves of similar quality observed at different times. Additional observations of AI Phe that will enable this test to be done are expected during Cycle 3 of the TESS mission. A less stringent test but one that is nevertheless important is to check that the detrending of the light curve has not biased the results. This can be done by comparing the values obtained for Runs A and S in which we analysed the PDCSAP_FLUX data and the SAP_FLUX data in the same way. The results from these two runs are consistent within their estimated errorbars, so we conclude that the detrending has not biased the results in this case.

The parameters from this study are within about 2 standard deviations of the quoted value and errors from previous studies. This level of agreement is quite satisfactory, given the difficulties in calculating the orbital phase for data from different observing seasons caused by the long and variable orbital period of AI Phe.

5.2 Limb darkening

Maxted (2018b) showed that the parameters $h_1 = I_\lambda(1/2)$ and $h_2 = I_\lambda(1/2) - I_\lambda(0)$ are useful for comparing the limb darkening measured from light curves of transiting exoplanets to model predictions because they are not strongly correlated with one another. Here, $I_\lambda(\mu)$ is the surface brightness relative to the value at the centre of the stellar disc, and μ is the cosine of the angle between the line

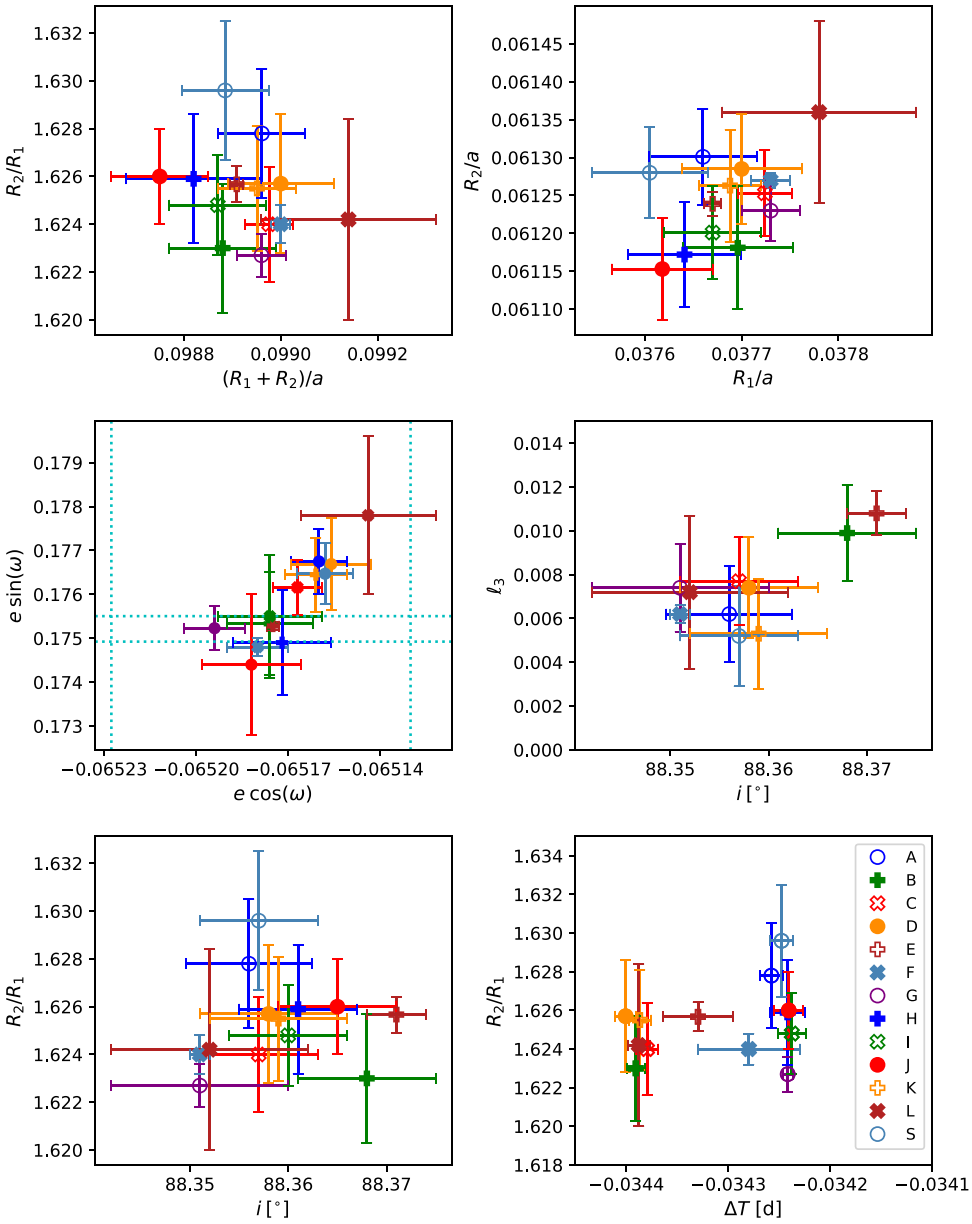

Figure 6. Parameters of AI Phe obtained from the TESS light curve using different light-curve models. The dashed lines in the plot of $e\sin\omega$ versus $e\cos\omega$ are the values determined from the spectroscopic orbits of Sybilski et al. (2018) and Gallenne et al. (2019). ΔT is the measured time of mid-eclipse relative to $\mathrm{BJD_{TDB}} = 2458\,362.862\,73$, the time of mid-eclipse predicted using the ephemeris from Kirkby-Kent et al. (2018).

of sight and the normal vector to the stellar surface. The power-2 limb-darkening law used by Maxted (2018b) is defined by $I_\lambda(\mu) = 1 - c(1-\mu^\alpha)$, so $h_1 = 1 - c(1-2^{-\alpha})$ and $h_2 = c2^{-\alpha}$. From Run A, we obtain the values $h_{1,\mathrm{F}} = 0.8167 \pm 0.0036$ and $h_{2,\mathrm{F}} = 0.61 \pm 0.11$ for star 1 (the F7 V star). Note that these parameters are constrained by Gaussian priors with standard deviations of 0.05 and 0.25 for h_1 and h_2, respectively. If we assume $T_{\mathrm{eff,F}} = 6310 \pm 100$ K, then interpolation in table 2 of Maxted (2018b) gives $h_{1,\mathrm{F}} = 0.818 \pm 0.004$ and $h_{2,\mathrm{F}} = 0.418 \pm 0.003$. The agreement between the observed and model values of $h_{1,\mathrm{F}}$ is remarkable and is consistent with the conclusion from Maxted (2018b) that the values of h_1 derived from the STAGGER-grid stellar atmosphere models (Magic et al. 2015) are accurate to about ± 0.01 for dwarf stars with $T_{\mathrm{eff}} \approx 6000$ K. The value of $h_{2,\mathrm{F}}$ does not fit with the trend observed in Maxted (2018b) for the observed values h_2 to be lower than the predicted values by about 0.05. However, the effect of $h_{2,\mathrm{F}}$ on the light curve of AI Phe is extremely subtle so a much more careful analysis of the systematic error in this value would be needed before drawing any firm conclusions. For the K0 IV star, we obtain the values $h_{1,\mathrm{K}} = 0.761 \pm 0.049$ and $h_{2,\mathrm{K}} = 0.63 \pm 0.12$ from Run A. The error on $h_{1,\mathrm{K}}$ is almost equal to the standard deviation of the Gaussian prior on this value, i.e. there is no constraint on this parameter from the light curve.

We also compared the quadratic limb-darkening coefficients, u_1 and u_2, obtained from Run D to the tabulated values calculated from stellar model atmospheres by Claret & Bloemen (2011). The values from the light-curve analysis are $u_1 = 0.252 \pm 0.024$, $u_2 = 0.246 \pm 0.053$ for the F7 V star and $u_1 = 0.409 \pm 0.036$, $u_2 =$

Table 4. Masses, radii, and derived parameters for the stars in AI Phe. Surface gravity, g, is given in cgs units, ρ is the mean stellar density, and $C(x, y)$ is the covariance of x and y.

Parameter	Value	
$M_1/\mathcal{M}^{\rm N}_\odot$	1.1938 ± 0.0008	[0.07 per cent]
$M_2/\mathcal{M}^{\rm N}_\odot$	1.2438 ± 0.0008	[0.06 per cent]
$R_1/\mathcal{R}^{\rm N}_\odot$	1.8050 ± 0.0022	[0.12 per cent]
$R_2/\mathcal{R}^{\rm N}_\odot$	2.9332 ± 0.0023	[0.08 per cent]
$\rho_1/\rho^{\rm N}_\odot$	0.20299 ± 0.00076	[0.38 per cent]
$\rho_2/\rho^{\rm N}_\odot$	0.04928 ± 0.00014	[0.29 per cent]
$\log g_1$	4.0020 ± 0.0011	[0.03 per cent]
$\log g_2$	3.5981 ± 0.0009	[0.03 per cent]
$C\left(M_1/{\rm M}^{\rm N}_\odot,\ M_2/{\rm M}^{\rm N}_\odot\right)$	5.89×10^{-7}	
$C\left(M_1/{\rm M}^{\rm N}_\odot,\ R_1/{\rm R}^{\rm N}_\odot\right)$	-1.51×10^{-7}	
$C\left(M_2/{\rm M}^{\rm N}_\odot,\ R_2/{\rm R}^{\rm N}_\odot\right)$	-1.04×10^{-6}	
$C\left(R_1/{\rm R}^{\rm N}_\odot,\ R_2/{\rm R}^{\rm N}_\odot\right)$	2.06×10^{-6}	

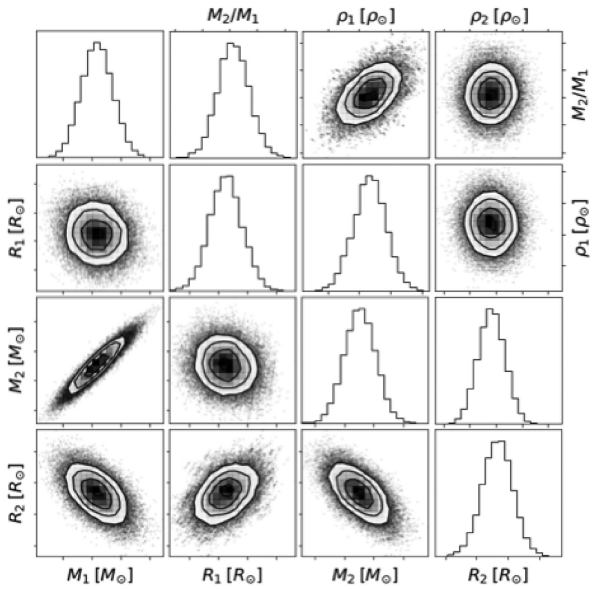

Figure 7. Parameter correlation plots for the mass, radius, and density of the stars in AI Phe.

0.237 ± 0.075 for the K0 IV star. Interpolating using parameters $T_{\rm eff,\,1} = 6310$ K, $T_{\rm eff,\,2} = 5010$ K, $\log g_1 = 4.00$, $\log g_2 = 3.60$, and [Fe/H]=−0.10, we obtain $u_1 = 0.210$, $u_2 = 0.307$ for the F7 V star and $u_1 = 0.392$, $u_2 = 0.219$ for the K0 IV star, which are consistent with the observed values to within 0.1.

The coefficients of the cubic limb-darkening law were found to be much less well constrained. Indeed, for a few of the simulated light curves used in the residual-permutation analysis the best-fitting light curve required coefficients that are not physically realistic. This may explain why the error estimates from Run L are noticeably larger than those from other analysis methods.

5.3 Times of mid-eclipse and third light.

We define the time of mid-eclipse to be the time when the angular separation on the sky between the centres of the two stellar discs is at a minimum (Lacy 1992). The times of mid-eclipse from Table 2 tend to fall into two groups – those near 2458 362.828 50 and another

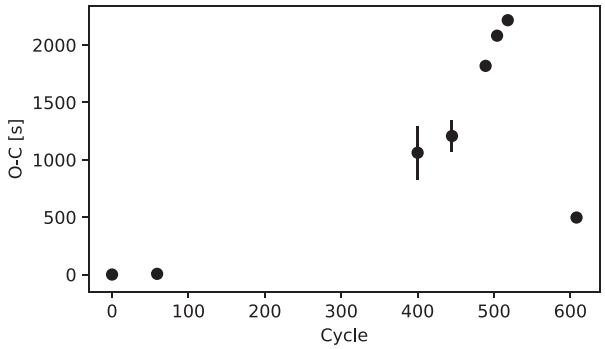

Figure 8. Residuals from the ephemeris of Hrivnak & Milone (1984) for times of mid-primary eclipse converted to $\rm BJD_{TDB}$. The ephemeris on this time system is $\rm BJD_{TDB} = 2443410.6891{+}24.592325 \times E$, where E is the cycle number.

group near 2458 362.828 34. The times of mid-eclipse near the latter value have, with the exception of Run G, been derived using either light-curve codes based on the EBOP algorithm or the WD algorithm. Inspection of the source code reveals that both these algorithms use the approximation $i = 90^\circ$ to calculate the mean anomaly at mid-primary eclipse. A similar approach was also used for Run G. For AI Phe, this approximation results in an offset of 0.000 13 d between the predicted and observed time of mid-eclipse. If we apply this correction then the unweighted mean time of mid-primary eclipse is 2458 362.828 50 with standard deviation of 0.000 02 d. Fig. 8 shows this time of minimum as a residual from the ephemeris of Hrivnak & Milone (1984). Note that all published times of minimum were converted to Barycentric Dynamical Time (TDB) for consistency with the timestamps used in the TESS archive data products (Tenenbaum & Jenkins 2018) prior to calculating the residuals shown in this figure. There has been a quite dramatic shift in the time of primary eclipse from this linear ephemeris since the observations obtained with the WASP instrument reported in Kirkby-Kent et al. (2016). This is likely to be due to the periastron passage of the putative third body in the system sometime between JD 2456000 and 2458000.

A complete dynamical analysis of the AI Phe system is beyond the scope of this paper, but may be worthwhile in order to better understand whether the third body might be a stellar remnant (e.g. white dwarf) or a low-mass star. A useful constraint in such an analysis is the observation that this third body is very faint compared to the eclipsing components. We used the broadening function method (Rucinski 1992) to look for any sign of third light in the HARPS spectra of AI Phe analysed by Gallenne et al. (2019). If we assume that the third light is due to an M-dwarf with $T_{\rm eff} \sim 3000$ K, then this star contributes no more than about 1 per cent of the optical flux. The interferometric observations reported in Gallenne et al. also enable us to put a limit of $H > 10.5$ for the magnitude of any resolved companions within 100 mas of the eclipsing binary. A third-light contribution of $\ell_3 = 0.7$ per cent in the TESS band would correspond to a K9V star at a distance of AI Phe. Such a star would have a H-band magnitude $H \approx 11.3$, which is consistent with this non-detection. Comparing the results for ℓ_3 in Table 3 to our estimate of 0.5 per cent for the contamination from the faint star seen in Fig. 1, we see that the third-body probably contributes no more than about 0.3 per cent of the flux in the TESS band. However, it should be noted that it is not clear how robust the estimate of ℓ_3 from the light-curve analysis is. For Runs H, I, and J, we find there is essentially no constraint on ℓ_3 within the uniform prior over the range [0, 0.05]

imposed during the MCMC analysis. This is in contrast to other runs which typically find $\ell_3 \approx 0.007 \pm 0.002$. The reason for this difference is not clear but appears not to have a significant impact on the results so we have not investigated this issue further.

5.4 Error estimates

The main parameters from the light-curve analysis of interest for the calculation of the masses and radii of the stars are r_1, r_2, and i. The standard error estimates for these parameters in Table 2 vary by a factor of 5 or more. Given the level of agreement between the different methods, it is clear that the error estimates produced by some methods are underestimated, sometimes severely so. This is a well-known problem for light-curve codes that calculate so-called formal error estimates based on a quadratic approximation for the dependence of χ^2 on the model parameters in the region of the best fit, e.g. the WD model used for Run E. Indeed, the Cramer–Rao theorem states that any unbiased estimator for the parameters will deliver a covariance matrix on the parameters that is no better than this (Albrecht et al. 2009).

6 CONCLUSIONS

The robustness of our results for AI Phe is partly due to the fact that the primary eclipse is total. This gives a direct measurement of the flux ratio for the binary from the depth of the eclipse where one star is completed occulted (Russell 1912). This key parameter can be strongly correlated with the radius ratio and inclination for systems with partial eclipses, particularly if the eclipses are shallow. We expect that the analysis of TESS light curves for other eclipsing binaries with deep or total eclipses will, in general, be similarly robust. For systems with partial eclipses, we recommend that the dependence of the results on assumptions such as the limb-darkening model, third light contribution, and detrending method used in the analysis should be careful examined and presented along with the parameters of interest.

The comparison of results obtained using different methods and analysed independently by different researchers has been illuminating. The results for the light-curve analysis presented here are typically not the first results that were produced by each analyst. An initial comparison of our results revealed a number of issues, some of which are described above. These issues generally have a small effect on the results but even small biases can be significant when working with space-based photometry. We strongly recommend that independent analysis using two or more methods are carried out and reported when using space-based photometry to characterize eclipsing binaries to high precision ($\lesssim$0.5 per cent).

The value of inspecting the residuals from the best light-curve fit should not be underestimated. We recommend that these residuals should always be clearly shown in any published analysis of an eclipsing binary as has been done here in Fig. 3. The residuals from the other best-fitting light-curve models presented here (with the exception of Run E) are equally good; that is, there is no noticeable increase in the scatter of the residuals through the eclipse cf. the out-of-eclipse phases, and no trends within the residuals indicative of a poor fit to the depth or shape of the eclipse. If this is not the case then some level of systematic error in the parameters derived from the model must be expected. This was found to be the case for AI Phe if we used a linear limb-darkening law to model the light curve.

The preferred method for estimating errors on the light-curve parameters is to analyse multiple independent data sets. If multiple orbits of the binary systems have been observed by one instrument this is easily achieved by analysing subsets of the data (e.g. Maxted 2018a; Hełminiak et al. 2019). Taking the standard error of the mean across subsets is a straightforward and robust way to estimate the error on each parameter if at least 3 (preferably 4) subsets can be created. This may also mitigate systematic errors in the results from imperfect model fits in some cases if the poor fit is caused by an effect that 'averages out' over multiple eclipses. For long-period binaries such as AI Phe where the light curve only covers one or two orbital cycles, Monte Carlo methods such as EMCEE or residual permutation can give realistic error estimates if used correctly, as can be seen in Fig. 6. The 'formal' errors obtained from the covariance matrix are certainly underestimates of the true uncertainty and should not be used.

The agreement between the masses obtained from spectra of AI Phe obtained at high resolution ($R > 60\,000$) with good S/N and good phase coverage is very good. This is an ideal case – both stars rotate slowly and so have narrow spectral lines and low levels of stellar activity. The accuracy of the masses may not be so good for rapidly rotating or magnetically active stars, particularly if there is a lack of spectra covering the key orbital phases when the stars are near their maximum and minimum RVs.

Differences between the various limb-darkening laws we have used is a significant contribution to the error in the radius in our analysis. It is not clear from this analysis which is the preferred limb-darkening law to use, although the linear limb-darkening approximation is certainly not accurate enough. We can expect progress to be made in our understanding of limb darkening for cool stars over coming years because the same issue also affects observational studies of transiting exoplanets. This problem can be tackled using high-quality light curves for transiting exoplanet systems and suitable eclipsing binaries from TESS and other space-based instrumentation.

ACKNOWLEDGEMENTS

This paper includes data collected by the TESS mission. Funding for the TESS mission is provided by the NASA Explorer Program. PM acknowledges support from Science and Technology Facilities Council, research grant no. ST/M001040/1. KGH acknowledges support provided by the Polish National Science Center through grant no. 2016/21/B/ST9/01613. AP acknowledges NASA support via grant no. 80NSSC18K0417 and NSF support via grant no. 1909109. This work has received funding from the European Research Council (ERC) under the European Union's Horizon 2020 research and innovation programme (CartographY GA. 804752). GRD, WB, and WJC acknowledge the support of the UK Science and Technology Facilities Council (STFC). The national facility capability for SkyMapper has been funded through ARC LIEF grant no. LE130100104 from the Australian Research Council, awarded to the University of Sydney, the Australian National University, Swinburne University of Technology, the University of Queensland, the University of Western Australia, the University of Melbourne, Curtin University of Technology, Monash University, and the Australian Astronomical Observatory. SkyMapper is owned and operated by The Australian National University's Research School of Astronomy and Astrophysics. The survey data were processed and provided by the SkyMapper Team at ANU. The SkyMapper node of the All-Sky Virtual Observatory (ASVO) is hosted at the National Computational Infrastructure (NCI). Development and support the SkyMapper node of the ASVO has been funded in part by Astronomy Australia Limited (AAL) and the Australian Government through the Commonwealth's Education Investment Fund (EIF) and National Collab-

orative Research Infrastructure Strategy (NCRIS), particularly the National eResearch Collaboration Tools and Resources (NeCTAR) and the Australian National Data Service Projects (ANDS). CJ recognizes support from the European Research Council (ERC) under the European Union's Horizon 2020 research and innovation programme (grant agreement no. 670519: MAMSIE), and from the Research Foundation Flanders (FWO) under grant no. G0A2917N (BlackGEM). Parameter correlation plots were generated using the PYTHON package `corner` (Foreman-Mackey 2016). We would like to thank the anonymous referee for their constructive and timely comments on the manuscript.

REFERENCES

Albrecht A. et al., 2009, preprint (arXiv:0901.0721)
Andersen J., Clausen J. V., Nordstrom B., Gustafsson B., Vandenberg D. A., 1988, A&A, 196, 128
Ball W. H., Chaplin W. J., Schofield M., Miglio A., Bossini D., Davies G. R., Girardi L., 2018, ApJS, 239, 34
Borkovits T., Rappaport S., Hajdu T., Sztakovics J., 2015, MNRAS, 448, 946
Castelli F., Kurucz R. L., 2003, in Piskunov N., Weiss W. W., Gray D. F., eds, Proc. IAU Symp. 210, Modelling of Stellar Atmospheres. Cambridge University Press, Cambridge, p. A20
Claret A., 2017, A&A, 600, A30
Claret A., Bloemen S., 2011, A&A, 529, A75
Davies G. R., Miglio A., 2016, Astron. Nachr., 337, 774
Etzel P. B., 1981, in Carling E. B., Kopal Z., eds, Photometric and Spectroscopic Binary Systems. D. Reidel Publishing Co., Dordrecht, p. 111
Foreman-Mackey D., 2016, J. Open Source Softw., 1, 24
Foreman-Mackey D., Hogg D. W., Lang D., Goodman J., 2013, PASP, 125, 306
Foreman-Mackey D., Agol E., Ambikasaran S., Angus R., 2017, AJ, 154, 220
Gallenne A. et al., 2019, A&A, 632, A31
Gelman A., Rubin D., 1992, Stat. Sci., 7, 457
Ghezzi L., Johnson J. A., 2015, ApJ, 812, 96
Gray R. O., 1999, Astrophysics Source Code Library, record ascl:9910.002
Hełminiak K. G., Konacki M., Ratajczak M., Muterspaugh M. W., 2009, MNRAS, 400, 969
Hełminiak K. G., Konacki M., Maehara H., Kambe E., Ukita N., Ratajczak M., Pigulski A., Kozłowski S. K., 2019, MNRAS, 484, 451
Hestroffer D., 1997, A&A, 327, 199
Higl J., Weiss A., 2017, A&A, 608, A62
Horvat M., Conroy K. E., Pablo H., Hambleton K. M., Kochoska A., Giammarco J., Prša A., 2018, ApJS, 237, 26
Hrivnak B. J., Milone E. F., 1984, ApJ, 282, 748
Imbert M., 1979, A&AS, 36, 453
Irwin J. M. et al., 2011, ApJ, 742, 123
Kipping D. M., 2016, MNRAS, 455, 1680
Kirkby-Kent J. A., Maxted P. F. L., Serenelli A. M., Turner O. D., Evans D. F., Anderson D. R., Hellier C., West R. G., 2016, A&A, 591, A124
Kirkby-Kent J. A., Maxted P. F. L., Serenelli A. M., Turner O. D., Evans D. F., Anderson D. R., Hellier C., West R. G., 2018, A&A, 620, C5
Lacy C. H. S., 1992, AJ, 104, 2213
Lastennet E., Valls-Gabaud D., 2002, A&A, 396, 551
Magic Z., Chiavassa A., Collet R., Asplund M., 2015, A&A, 573, A90
Maxted P. F. L., 2016, A&A, 591, A111
Maxted P. F. L., 2018a, Res. Notes Am. Astron. Soc., 2, 39
Maxted P. F. L., 2018b, A&A, 616, A39
Orosz J. A., Hauschildt P. H., 2000, A&A, 364, 265
Paxton B. et al., 2018, ApJS, 234, 34
Pols O. R., Tout C. A., Schroder K.-P., Eggleton P. P., Manners J., 1997, MNRAS, 289, 869
Popper D. M., Etzel P. B., 1981, AJ, 86, 102
Press W. H., Teukolsky S. A., Vetterling W. T., Flannery B. P., 1992, Numerical Recipes in FORTRAN: The Art of Scientific Computing. Cambridge Univ. Press, Cambridge
Prša A., 2018, Modeling and Analysis of Eclipsing Binary Stars: The Theory and Design Principles of PHOEBE. IOP Publishing, Ltd., Bristol
Prša A., Zwitter T., 2005, in Turon C., O'Flaherty K. S., Perryman M. A. C., eds, ESA SP-576: The Three-Dimensional Universe with Gaia, ESA, p. 611
Prša A., Zwitter T., 2005, ApJ, 628, 426
Prša A. et al., 2016, ApJS, 227, 29
Prša A. et al., 2016, AJ, 152, 41
Rauer H. et al., 2014, Exp. Astron., 38, 249
Reipurth B., 1978, Inf. Bull. Var. Stars, 1419, 1
Ribas I., Jordi C., Giménez Á., 2000, MNRAS, 318, L55
Ricker G. R. et al., 2015, J. Astron. Telesc. Instrum. Sys., 1, 014003
Rucinski S. M., 1992, AJ, 104, 1968
Russell H. N., 1912, ApJ, 35, 315
Schofield M. et al., 2019, ApJS, 241, 12
Short D. R., Orosz J. A., Windmiller G., Welsh W. F., 2018, AJ, 156, 297
Skilling J., et al., 2006, Bayesian Anal., 1, 833
Southworth J., 2008, MNRAS, 386, 1644
Southworth J., 2013, A&A, 557, A119
Southworth J., Maxted P. F. L., Smalley B., 2004, MNRAS, 351, 1277
Spada F., Demarque P., Kim Y. C., Sills A., 2013, ApJ, 776, 87
Strohmeier W., 1972, Inf. Bull. Var. Stars, 665, 1
Sybilski P., Pawłaszek R. K., Sybilska A., Konacki M., Hełminiak K. G., Kozłowski S. K., Ratajczak M., 2018, MNRAS, 478, 1942
Tenenbaum P., Jenkins J. M., 2018, Technical Report, TESS Science Data Products Description Document. TESS Program Office, NASA Goddard
Ter Braak C. J., 2006, Stat. Comput., 16, 239
Van Hamme W., Wilson R. E., 2007, ApJ, 661, 1129

This paper has been typeset from a TEX/LATEX file prepared by the author.